ROYAL SOCIETY
OF CHEMISTRY

PAPER

CrossMark
← click for updates

Self-oriented Sb$_2$Se$_3$ nanoneedle photocathodes for water splitting obtained by a simple spin-coating method†

Jimin Kim,‡[a] Wooseok Yang,‡[a] Yunjung Oh,[a] Hyungsoo Lee,[a] Seonhee Lee,[b] Hyunjung Shin,[b] Joosun Kim[c] and Jooho Moon*[a]

Synthesis of one-dimensional nanostructured chalcogenide compounds using nontoxic and abundant constituents provides an important pathway to the development of commercially feasible photoelectrochemical water splitting. In this study, grass-like Sb$_2$Se$_3$ nanoneedle arrays are successfully fabricated on a substrate *via* a facile spin-coating method without any complicated processes such as templating, seed formation, or use of a vapor phase. Preferential [001] growth of the initial single-crystalline Sb$_2$Se$_3$ occurs during the first spin-coating, but interfacial defects are generated upon subsequent spin-coating iterations, resulting in annual-ring-like growth of Sb$_2$Se$_3$ nanoneedles. After sequential surface modification with TiO$_2$ and Pt, the resistance to charge transfer from the photoelectrode to the electrolyte decreases significantly, yielding a remarkable record-high photocurrent of 2 mA cm^{-2} at 0 V$_{RHE}$ (4.5 mA cm^{-2} at −0.2 V$_{RHE}$).

Introduction

Exploring new absorber materials consisting of nontoxic and abundant constituents has been of great interest for economically feasible solar energy conversion. Although Cu(In,Ga)Se$_2$, CdTe, and organic–inorganic metal halide perovskites (for example, CH$_3$NH$_3$PbI$_3$) have been considered promising next-generation light-absorbing materials, their toxic and/or expensive elements hinder commercialization.[1–3] FeS$_2$ and Cu$_2$ZnSnS$_2$, which are known as low-cost and nontoxic absorbers, have complex compositions, so they easily form secondary phases such as FeS, CuS$_2$, and ZnS.[4–6] On the other hand, another low-cost light absorber, antimony triselenide (Sb$_2$Se$_3$), has only a thermodynamically stable orthorhombic phase.[7] Sb$_2$Se$_3$, which has promising optical and electrical properties, has been applied in optoelectronic devices such as solar cells,[8]

photodetectors,[9] and thermoelectric devices,[10] and photoelectrochemical (PEC) applications.[11]

One-dimensional (1D) semiconductor nanostructures including nanotubes, nanorods, nanowires, and arrays of these structures have been extensively investigated because of their desirable optoelectronic properties including short transport distances for photogenerated carriers, large specific surface areas, and efficient optical absorption.[12–14] A variety of nanostructures of Sb$_2$Se$_3$ such as nanorods, nanoribbons, nanowires, and hierarchical structures have been synthesized by a solvothermal route, a surfactant- or polymer-derived hydrothermal technique, microwave-assisted synthesis, and liquid–solid spinodal decomposition.[10,15–19] However, hydrothermal/solvothermal methods are generally time-consuming, and microwave-assisted synthesis requires expensive and complex equipment. Furthermore, the complex growth mechanism of spinodal decomposition inevitably involves complex heating profiling, resulting in nonuniform phase segregation.

Herein, we report a novel method for synthesizing Sb$_2$Se$_3$ nanoneedles *via* a simple solution process. Grass-like Sb$_2$Se$_3$ nanoneedle arrays on a conductive substrate were obtained by facile spin-coating and heating without any complicated processes such as templating, seed formation, or use of a liquid or gas phase, which are commonly implemented for nanostructuring.[12] Subsequent deposition of TiO$_2$ on the simply fabricated Sb$_2$Se$_3$ and surface decoration with Pt allow us to fabricate an Sb$_2$Se$_3$-based photocathode that exhibits enhanced performance, reaching a record-high photocurrent density of 2 mA cm^{-2} at 0 V *versus* a reversible hydrogen electrode (RHE, V$_{RHE}$).

[a]Department of Materials Science and Engineering, Yonsei University, 50 Yonsei-ro Seodaemun-gu, Seoul 120-749, Republic of Korea. E-mail: jmoon@yonsei.ac.kr

[b]Department of Energy Science, Sungkyunkwan University, 2066 Seobu-ro, Jangan-gu, Suwon 440-746, Republic of Korea

[c]High-Temperature Energy Materials Research Center, Korea Institute of Science and Technology, Seoul 136-791, Republic of Korea

Results and discussion

Sb–Se precursor solutions were prepared as shown in Fig. 1. Se solutions were obtained by dissolving Se powder in a cosolvent of thioglycolic acid (TGA) and ethanolamine (EA), and $SbCl_3$ was dissolved in 2-methoxyethanol (2 ME) to prepare Sb solutions. After the two solutions were mixed; the resulting murky red solution gradually changed to a clear red solution. This experimental observation suggests that chemical reactions such as complexation and chelation between the Se, TGA, and/or Sb components occurred in the solution phase, as previously observed in the precursor solution for chalcogenide materials.[20,21] Fig. 2 shows top-view scanning electron microscopy (SEM) images of annealed Sb_2Se_3 as a function of annealing temperature from 100 to 350 °C. Interestingly, as-dried Sb_2Se_3 already revealed 1D morphology when dried at 130 °C without any complex processing. With increasing annealing temperature, the needle shape became sharp and distinct because of solvent evaporation, excess Se loss, and decomposition of NH_4Cl. One plausible origin for the self-oriented nanostructure is the intrinsic anisotropy of Sb_2Se_3. The anisotropy results from the different bonding characteristics of the chain-like layered structure, where strong covalent bonding occurs along the *c* crystallographic axis, and much weaker van der Waals bonding occurs between the chains.[22] This bonding anisotropy is known to be a driving force for the synthesis of 1D nanostructures in which Sb_2Se_3 has a preferred [001] crystal growth direction.[15–17,19] Despite the intrinsic anisotropy of Sb_2Se_3, however, Sb_2Se_3 thin films were also reportedly obtained using a hydrazine-based solution process, electrodeposition, chemical bath deposition, reactive pulsed laser deposition, or thermal evaporation.[8,11,22–24] Thus, we can assume that an additional factor also contributes to the self-oriented nanostructure. A possible explanation for the self-oriented nanostructure is that TGA can act as a capping agent that is adsorbed on a certain crystallographic plane of the initially formed nanocrystals, providing preferential growth of [001]-oriented Sb_2Se_3 nanoneedles. Many similar examples have been found in which TGA can play a crucial role in the growth of 1D nanostructures.[25–27] However, other chalcogenide materials such as Cu_2ZnSnS_4, which were derived from a similar solvent system incorporating a mixed solution of TGA, EA, and 2 ME, revealed a thin film morphology.[28] Therefore, it is reasonable to assume that

a combination of the intrinsic anisotropy in Sb_2Se_3 and the specific chemical interaction yields a unique self-oriented nanostructure in the present work. The detailed chemistry of the precursor solution, in conjunction with the formation mechanism of self-oriented Sb_2Se_3 nanoneedles, will be elucidated in a future study.

The morphological evolution of the Sb_2Se_3 nanoneedles as a function of the number of spin-coating iterations was examined, and representative nanoneedles obtained after each spin-coating are shown in Fig. 3a. After the first spin-coating, Sb_2Se_3 had a nanorod structure with a uniform thickness of 40 nm and length of 300 nm. After the second coating, the Sb_2Se_3 exhibited needle-like structures that grew continually in both the axial and radial directions with increasing number of spin-coating iterations. However, the diameter remained almost unchanged after the third spin-coating because spatial constraints between the inclined Sb_2Se_3 nanoneedles interrupted further growth in diameter, whereas axial growth proceeded with increasing number of spin-coating iterations. To obtain reliable statistics regarding the length and diameter of the Sb_2Se_3 nanoneedles, we analyzed about 30 nanoneedles, which are shown in SEM images in Fig. S1 (ESI†); the statistics are shown in Fig. 3b and c. A cross-sectional SEM image (Fig. S2, ESI†) reveals grass-like Sb_2Se_3 nanoneedle arrays. Fig. 3d shows a schematic diagram of the possible formation mechanism of the nanoneedles. During multiple coatings, the precursor solution wets the pre-existing nanoneedles, and the capillary-force-induced preferential wetting of the lower part of the nanoneedles leads to carrot-like nanoneedle growth. Fig. S3 (ESI†) shows the X-ray diffraction (XRD) patterns of the Sb_2Se_3 nanoneedle arrays after they were annealed at different temperatures on a gold-coated fluorine-doped tin oxide (FTO) substrate. Crystalline Sb_2Se_3 peaks appeared after annealing at 180 °C, and all the diffraction peaks in the XRD pattern can be readily indexed to orthorhombic Sb_2Se_3 (JCPDS Card no. 15-0817). The peaks for Sb_2Se_3 maintained roughly constant intensity, whereas the peaks for the Au layer ($2\theta = 38.5°$ and $44.7°$) increased with increasing annealing temperature, indicating that the crystallinity of Sb_2Se_3 remained close to its initial state despite the rise in the annealing temperature.

Transmission electron microscopy (TEM), scanning transmission electron microscopy (STEM) and energy-dispersive X-ray spectroscopy (EDS) were performed to determine the microstructure and composition of individual synthesized Sb_2Se_3 nanoneedles. Fig. 4a shows a TEM image of a representative Sb_2Se_3 nanoneedle. The cross-sectional image (inset) revealed concentric circles, indicating the formation of an annual-ring-like inner structure in the Sb_2Se_3 nanoneedles. Fig. 4b and c show high-resolution TEM images and the corresponding fast Fourier transform (FFT) images of the upper and lower parts of an Sb_2Se_3 nanoneedle, which are marked b and c, respectively, in Fig. 4a. The interplanar *d*-spacing of 0.39 nm can be indexed to the (001) plane of Sb_2Se_3 with an orthorhombic crystal structure regardless of the observation point. For the lower part, however, a defective structure was observed in the FFT images, whereas the diffraction spots for the upper part represented a perfect single crystal. Fine structures such as
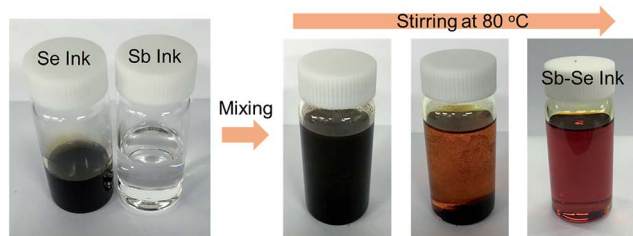

Fig. 1 Photographs showing synthesis of Sb–Se precursor solution. Se solution was obtained by dissolving Se powder in a cosolvent of thioglycolic acid and ethanolamine, and $SbCl_3$ was dissolved in 2-methoxyethanol to prepare Sb solution.
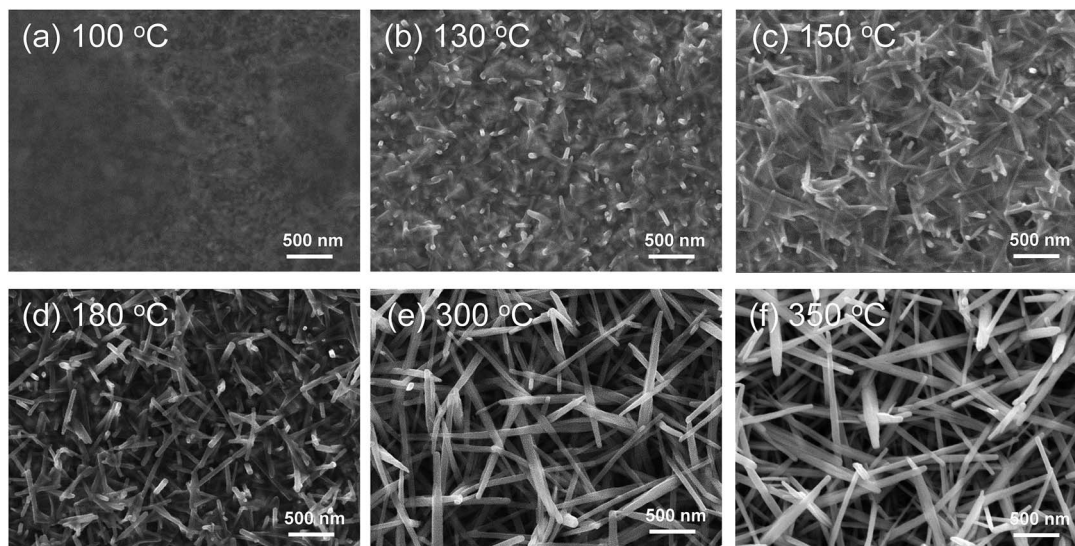
Fig. 2 Top-view SEM images of Sb_2Se_3 nanoneedles annealed at various temperatures.

streaks and extra spots in the diffraction patterns indicate the presence of crystal defects such as dislocations, twins, and stacking faults.[29] Here, the extra diffraction spots can be attributed to interfacial defects formed in the nanoneedle during multiple spin-coating iterations. The formation of defective interfaces during multiple spin-coatings was also supported by the selected area electron diffraction (SAED) pattern of an Sb_2Se_3 nanorod after the first spin-coating, which clearly revealed perfect single-crystallinity (Fig. S4, ESI†).

Streaks appeared after two spin-coatings, as shown in Fig. S5.† The STEM-EDS elemental mapping images showed uniform distributions of all the constituent elements of Sb_2Se_3 throughout the nanorod or nanoneedle regardless of the number of coating iterations (Fig. 4d, S4 and S5, ESI†). Quantitative EDS analysis was used to determine the Sb/Se composition ratio. The atomic ratio of Sb/Se was 1/1.61, which is close to that of stoichiometric Sb_2Se_3. These TEM analyses indicate that an initial single-crystalline Sb_2Se_3 nanorod grew
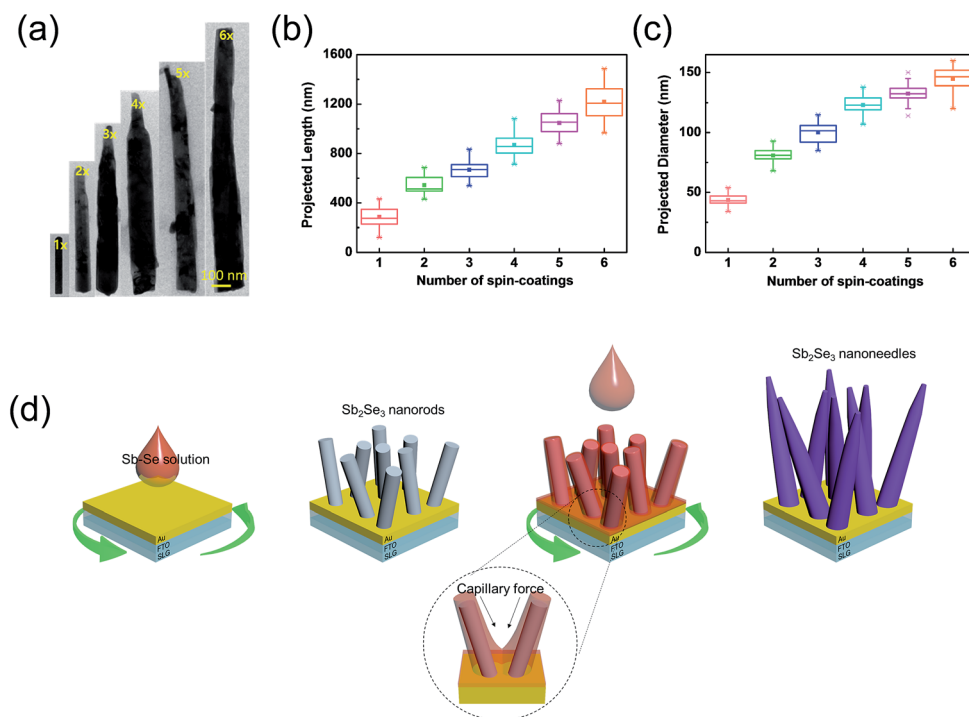

Fig. 3 (a) Representative individual Sb_2Se_3 nanoneedles after one to six spin-coating iterations (left to right). Statistics of (b) projected length and (c) diameter of Sb_2Se_3 nanoneedles as a function of the number of spin-coatings. Squares represent average values, and crosses show the maximum and minimum values. (d) Schematic diagram showing the growth process of the Sb_2Se_3 nanoneedles.
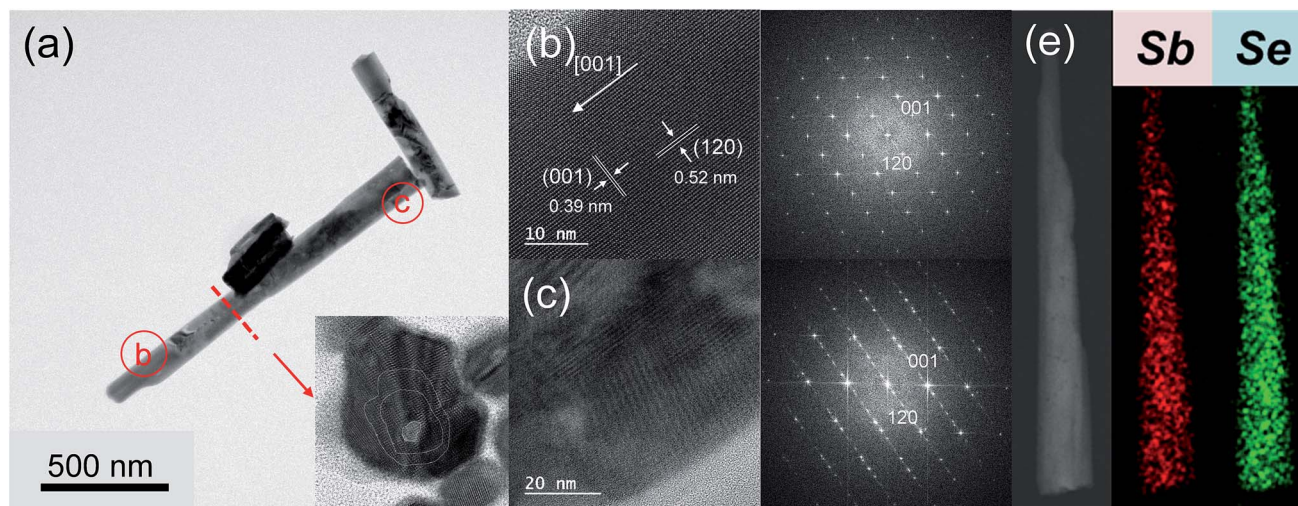
Fig. 4 (a) Low-resolution TEM image of a single Sb_2Se_3 nanoneedle (coated six times) and cross-sectional microstructure of the nanoneedle sectioned by a focused ion beam (inset). White lines delineate annual-ring-like growth. (b and c) High-resolution TEM images taken in regions marked b and c in (a), with the corresponding FFT images. (d) High-angle annular dark-field (HAADF)-STEM image and the corresponding EDS elemental mappings of Sb and Se.

preferentially in the [001] direction during the first spin-coating, but defective structures formed at the interfaces upon subsequent spin-coatings of the precursor solution, resulting in annual-ring-like growth of an Sb_2Se_3 nanoneedle.

The PEC performance of Sb_2Se_3 nanoneedle arrays was evaluated as a function of the annealing temperature and number of spin-coating iterations (Fig. 5). The measurement was conducted in 0.5 M H_2SO_4 electrolyte using linear sweep voltammetry under intermittent light illumination (AM 1.5G, 100 mW cm^{-2}). For all the samples, the Sb_2Se_3 nanoneedles were identified as p-type semiconductors because their photocurrent density increased with increasing cathodic potential. The photocurrent density, which can be determined by the difference between dark and light current, increased with increasing annealing temperature owing to the absence of undesirable residual phases such as excess Se, carbon impurities, and NH_4Cl. The optimum coating number was determined to be 6 because the Sb_2Se_3 nanoneedle array that was coated six times generated the largest photocurrent: 320 μA cm^{-2} at 0 V *versus* RHE. An n-type overlayer is commonly coated on the surface of a p-type photocathode to facilitate charge separation by forming a p–n junction as well as to protect the p-type semiconductor from photo- and electro-corrosion by preventing direct contact with the electrolyte.[30] We deposited an n-type TiO_2 layer by atomic layer deposition (ALD), which is a well-known technique for conformal coating of delicate nanostructures. The schematic of the band diagram depicting the energetics of the TiO_2/Sb_2Se_3 photocathode before/after equilibrium in the electrolyte is presented in Fig. S6 in ESI.† The fermi level and band position of Sb_2Se_3 and TiO_2 are reported in the literature.[31,32] In a schematic diagram, the equilibration would lead to form a type-II heterojunction where the electrons can selectively transfer from Sb_2Se_3 to the electrolyte through the TiO_2.

The SEM images in Fig. 6a and b show a blunt nanoneedle array that appeared after the TiO_2 layer was deposited. It was

found that the TiO_2 layer is amorphous, and the interface between TiO_2 and Sb_2Se_3 is of high quality (Fig. 6c and d). Elemental mapping of the TiO_2 and Sb_2Se_3 revealed conformal deposition of an oxide layer around a nanoneedle with
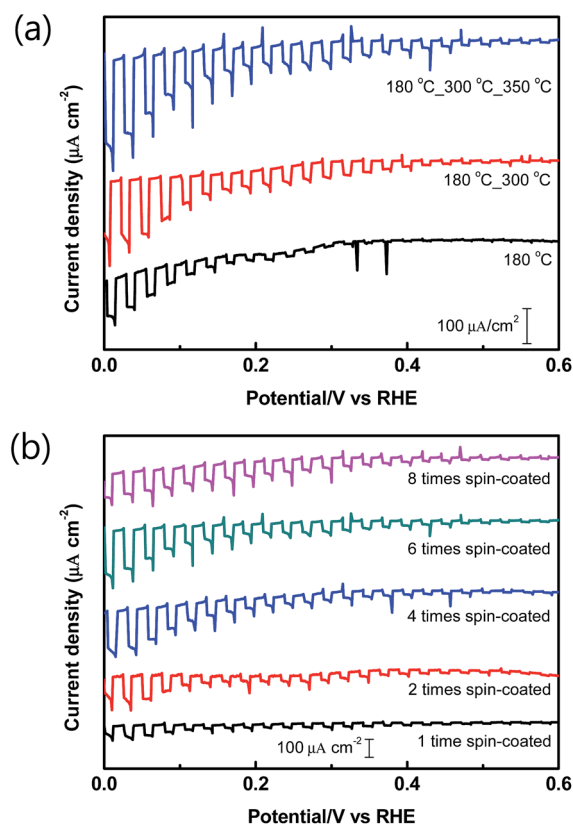

Fig. 5 PEC measurement in 0.5 M H_2SO_4 electrolyte for the Sb_2Se_3-nanoneedle-based device as a function of (a) annealing temperature and (b) number of spin-coating iterations.
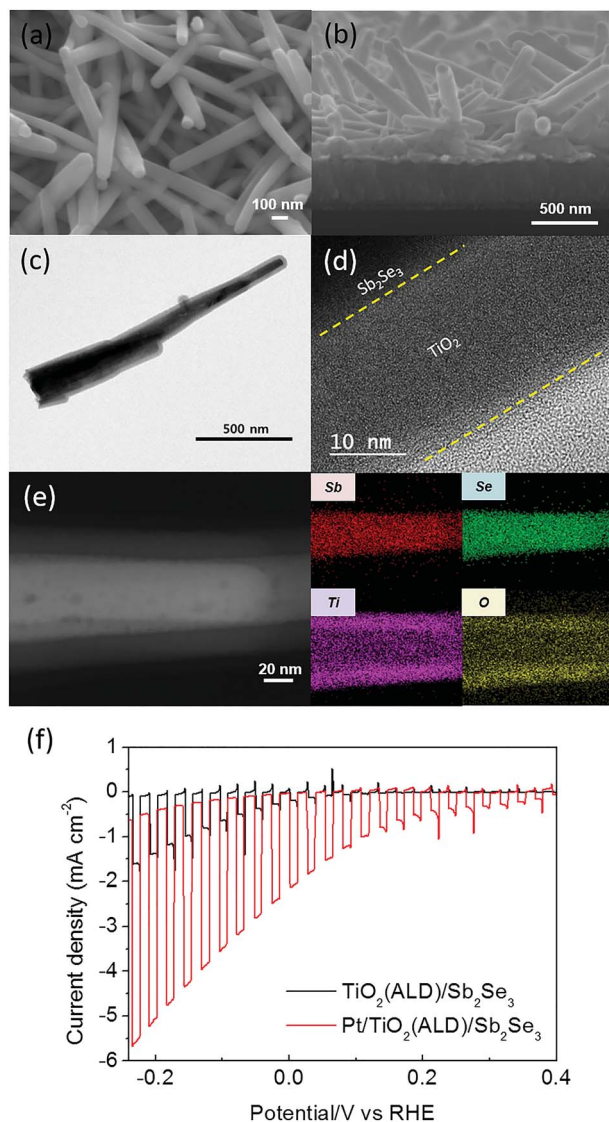
Fig. 6 (a) Top-view and (b) side-view SEM images of Sb_2Se_3 nanoneedles modified with TiO_2. (c) Low-resolution TEM image and (d) high-resolution TEM image of TiO_2/Sb_2Se_3. (e) HAADF-STEM image and the corresponding EDS elemental mapping of TiO_2/Sb_2Se_3. (f) PEC measurements of TiO_2/Sb_2Se_3 and $Pt/TiO_2/Sb_2Se_3$.

a thickness of ∼20 nm, as shown in Fig. 6e. Fig. 6f shows the PEC performance of the Sb_2Se_3 photocathode with n-type TiO_2 and Pt as a cocatalyst. Note that Pt is well known as an electrocatalyst which has very low overpotential for hydrogen evolution, showing near 30–40 mV at 10 mA cm^{-2}. The photocurrent improved significantly after both TiO_2 and Pt were deposited, indicating enhanced charge separation and catalytic properties for hydrogen evolution. The photocurrent density of $Pt/TiO_2/Sb_2Se_3$ reached 2 mA cm^{-2} at 0 V_{RHE} and 4.5 mA cm^{-2} at −0.2 V_{RHE}, which is a record for Sb_2Se_3-based photocathodes. Note that a previously reported Sb_2Se_3 thin film obtained by the photoelectrochemical method revealed only 0.05 mA cm^{-2} near 0 V_{RHE} in the same electrolyte (0.5 M H_2SO_4).[11]

In addition to the improvement in the photocurrent, a large shift in the onset potential was detected, as shown in Fig. S7

(ESI†). Deposition of Pt on TiO_2/Sb_2Se_3 led to a significant shift in the onset potential to 0.75 V_{RHE} compared to that of TiO_2/Sb_2Se_3 (0.47 V_{RHE}). This shift is useful for developing zero-bias tandem cells.

To elucidate the role of the n-type layer, we performed electrochemical impedance spectroscopy (EIS) in a frequency range of 300 kHz to 0.05 Hz under simulated solar light illumination at −0.1 V_{RHE}. The Nyquist plots of Sb_2Se_3 and TiO_2/Sb_2Se_3 are presented in Fig. S8 (ESI†). For detailed analysis, the EIS data were fitted to a simple equivalent circuit model of one series resistance (R_s) and two resistor–capacitor circuits consisting of a resistance (R) and a constant phase element (CPE). According to the recent EIS analysis of a PEC cell for water splitting,[33] R_s can be ascribed to the resistance of the conductive substrate (Au/FTO) and the first semicircle in the high-frequency region is attributed to the charge transport resistance within the electrode (R_1) with the capacitance of the bulk semiconductor (CPE_1). For other arcs in the low-frequency range, R_2 and CPE_2 elements characterize the charge transfer resistance and the capacitance of the electrode–electrolyte interface, respectively. The resistance corresponding to charge transfer (R_2) was greatly reduced after the n-type TiO_2 was deposited, whereas R_1 did not change much. This implies that as the band bending is increased by p–n junction formation, the inherent internal field that pulls photogenerated carriers away becomes stronger, thus reducing the amount of recombination. In general, charge separation and extraction are key elements for determining the energy conversion efficiency of PEC cells, and they are often limited by the kinetically sluggish surface reactions.[30] The greatly reduced charge transfer resistance observed in the EIS spectra is in good agreement with the enhanced PEC performance as discussed in the literature.[34–36] In addition to performing EIS, we measured the photoluminescence (PL) spectra of Sb_2Se_3 and TiO_2/Sb_2Se_3 (Fig. S9, ESI†). The PL emission from Sb_2Se_3 is a consequence of band-to-band radiative recombination of photogenerated charge carriers. The use of a contacting n-type layer results in quenching of the PL from Sb_2Se_3. Analysis of the PL quenching behavior provides information about the rate of charge injection into the n-type material from Sb_2Se_3 with respect to that of recombination of photoinduced charges within Sb_2Se_3. The relative PL quenching for the TiO_2/Sb_2Se_3 electrode was considerably greater than that for Sb_2Se_3, indicating reduced recombination by p–n junction formation. Furthermore, we can estimate the band gap from the PL emission peak. The experimentally determined band gap was 1.28 eV, which agreed well with the theoretical value. These EIS and PL analyses clearly demonstrate that TiO_2 deposition enables enhanced PEC performance.

Stable operation of the photocathode is a crucial factor for practical application in a PEC device. Thus, the stabilities of the Sb_2Se_3 nanoneedle arrays with and without TiO_2 and Pt were further evaluated using chronoamperometric measurements (Fig. S10, ESI†) at 0 V *versus* RHE. Before the Sb_2Se_3 was modified with TiO_2, its photoresponse was quite unstable, as previously reported, presumably owing to photocorrosion of Sb_2Se_3 in the electrolyte (Fig. S10a†). In contrast, the TiO_2/Sb_2Se_3 sample exhibited stable repeated on/off behavior for 4 h, as

2184 | *J. Mater. Chem. A*, 2017, **5**, 2180–2187

This journal is © The Royal Society of Chemistry 2017

shown in Fig. S10b (ESI†), indicating the protective role of the conformal TiO_2 layer. For the $Pt/TiO_2/Sb_2Se_3$ sample, the photocurrent decreased under extended monitoring, despite its initially high photocurrent. This degradation is likely caused by catalytic deactivation of Pt due to detachment or poisoning by anions such as S^{2-} and Se^{2-}.[37] Thus, further optimization of the cocatalyst is necessary to realize stable Sb_2Se_3-based photocathodes while retaining a remarkable photocurrent. One of the practical methods is the adoption of other deposition methods for Pt, such as photoelectrochemical deposition which is widely used in stable photocathodes.[38,39] Another possible alternative is to use non-novel metal catalysts such as MoS_x. For example, Carlos G. Morales-Guio et al. reported that the photocathode with a MoS_x co-catalyst reveals better stability than the Pt-deposited photocathode.[40] Further optimization of co-catalyst loading is currently under investigation and will be reported in our future study.

The amount of evolved H_2 from the $Pt/TiO_2/Sb_2Se_3$ photocathode was evaluated in a three-electrode configuration at 0 V vs. RHE under AM 1.5G radiation by gas chromatography (GC). Fig. S9 in the ESI† shows the typical time course curves for both H_2 evolution from the photocathode and one-half of the electrons passing through the outer circuit ($e^-/2$) as expressed by a solid line. The slope of the solid line decreased after 20 min due to the degraded photo-activity of the $Pt/TiO_2/Sb_2Se_3$ photocathode as discussed in Fig. S10 in the ESI.† The faradaic efficiency, which is the ratio of the rate of H_2 evolution to that of $e^-/2$, was close to unity (90–100%) after a short (ca. 20 min) induction period. The origin of the induction period in the H_2 measurement was likely due to the adhesion of the generated H_2 in the initial stage as discussed in the literature.[41] The faradaic efficiency indicated the absence of side reactions.

Experimental

Preparation of Sb_2Se_3 nanoneedles

The Sb_2Se_3 precursor solution was prepared by mixing an Sb solution with a Se solution. The Sb solution was obtained by dissolving 0.1 M $SbCl_3$ (99.99%, Alfa Aesar, Heysham, UK) in 12 mL of 2 ME (99.5%, Sigma Aldrich), and 0.405 g of Se powder (99.5%, Sigma Aldrich, St. Louis, MO, USA) was dissolved in a cosolvent of 5.3 mL of EA (99.5%, Sigma Aldrich) and 2.7 mL of TGA (98%, Sigma Aldrich) to prepare the Se solution. The mixture of the two solutions was magnetically stirred on an 80 °C hot plate inside a N_2-filled glovebox until the murky red solution changed to a clear red precursor solution. For Sb_2Se_3 fabrication, the precursor solution was deposited by spin-coating at 2000 rpm for 30 s under a N_2 atmosphere onto FTO glass (TEC-15, Pilkington, UK) coated with 60 nm-thick thermally evaporated Au. To investigate the effect of annealing temperature (Fig. 2), the as-spin-coated films were immediately dried at 100–180 °C for 3 min on a preheated hot plate. The procedure was repeated six times. For samples annealed over 300 °C (Fig. 2e–f), further annealing at 300 °C for 3 min and 350 °C for 20 min was performed for the samples dried at 180 °C (Fig. 2d). Hereafter the drying temperature was fixed at 180 °C

and the final annealing was performed at 350 °C for other characterizations including XRD, TEM and PEC performance.

Deposition of TiO_2 on the Sb_2Se_3 nanoneedles by ALD

An n-type TiO_2 layer was deposited on the Sb_2Se_3 nanoneedles by ALD. ALD precursors of tetrakis(dimethylamino) titanium (TDMAT, Easychem, Korea) and H_2O were employed as the Ti and O sources, respectively. N_2 gas was used as a carrier and purge gas. The deposition temperature was 160 °C, and TDMAT was evaporated at 45 °C. One ALD cycle consisted of 3/20 s of TDMAT injection/exposure followed by 15 s of N_2 purging and 2/5 s of H_2O injection/exposure followed by 20 s of N_2 purging. Four hundred deposition cycles were used to obtain 20 nm thickness. After deposition, the Sb_2Se_3 nanoneedles modified with TiO_2 were annealed at 200 °C in air. A Pt catalyst was also deposited on the photoelectrode by using a 108 Auto Sputter Coater (Ted Pella, Redding, CA, USA) under an applied current of 10 mA for 120 s.

Characterization

The morphology of the nanoneedle arrays was studied using field emission SEM (JSM-7800F, JEOL, Tokyo, Japan) in conjunction with EDS and TEM (Talos F200X, FEI, Hillsboro, OR, USA). Phase analysis of the Sb_2Se_3 nanoneedles was performed using XRD (SmartLab, Rigaku, The Woodlands, TX, USA) with Cu K_α radiation ($\lambda = 0.15406$ nm). PL analysis was performed using MAPLE-II (DongWoo Optron, Gwangju, Korea).

Photoelectrochemical measurements

Electrodes for PEC characterization were fabricated from the prepared Sb_2Se_3 nanoneedles as follows. A copper wire was connected to a conductive epoxy to form the back contact of the device, and the unnecessary parts of the electrode were then covered with epoxy resin (HYSOL 9642, Henkel, Düsseldorf, Germany). The electrochemical measurements and EIS were conducted in a typical three-electrode configuration using a potentiostat (SI 1287, Solartron, Leicester, UK). All of the potentials were referenced to a Ag/AgCl/sat. KCl reference electrode, and a Pt wire was used as the counter electrode. The PEC measurement used simulated solar light illumination (AM 1.5G, Newport Corporation) while the PEC cell was submerged in a 0.5 M aqueous H_2SO_4 solution. In all the measurements, the applied potentials were referred to the RHE to enable comparison with other reports. The following equation was employed to convert the potential:

$$E_{RHE} = E_{Ag/AgCl} + 0.059pH + 0.2$$

EIS measurement was performed in a frequency range of 300 kHz to 0.05 Hz under simulated solar light illumination at −0.1 V_{RHE}.

For H_2 detection, all cell compartments were thoroughly sealed in a quartz tube with a rubber septum to prevent any gas leakage. During irradiation, the headspace gas (150.00 ± 0.01

mL) of the reactor was intermittently sampled by using a gas-tight syringe and analyzed for H_2 using a gas chromatograph (6500GC system, YL Instrument, Anyang, Korea) equipped with a pulsed discharge detector (PDD) and a molecular sieve column.

Conclusions

We successfully fabricated grass-like Sb_2Se_3 nanoneedle arrays on a substrate *via* a facile spin-coating method without any complicated processing. During the first spin-coating, a single-crystalline Sb_2Se_3 nanorod was generated, and it grew to a carrot-like nanoneedle morphology upon repeated spin-coating iterations. The self-oriented Sb_2Se_3 nanoneedles consisted of an annual-ring-like inner structure with a preferred [001] growth orientation and defective structures at the interface formed by subsequent precursor coating. With further sequential deposition of n-type TiO_2 and Pt as cocatalysts, a remarkable photocurrent of 4.5 mA cm^{-2} at -0.2 V$_{RHE}$ was obtained, and the role of the n-type layer was elucidated by EIS and PL analyses. Our simple new synthetic method for fabricating grass-like nanostructures will pave the way to advances in nanotechnology as well as development of feasible nano-structured solar energy conversion devices.

Acknowledgements

Notes and references

1 A. Chirilă, S. Buecheler, F. Pianezzi, P. Bloesch, C. Gretener, A. R. Uhl, C. Fella, L. Kranz, J. Perrenoud, S. Seyrling, R. Verma, S. Nishiwaki, Y. E. Romanyuk, G. Bilger and A. N. Tiwari, *Nat. Mater.*, 2011, **10**, 857–861.

2 J. M. Burst, J. N. Duenow, D. S. Albin, E. Colegrove, M. O. Reese, J. A. Aguiar, C.-S. Jiang, M. K. Patel, M. M. Al-Jassim, D. Kuciauskas, S. Swain, T. Abelkim, K. G. Lynn and W. K. Metzger, *Nat. Energy*, 2016, **1**, 16015.

3 M. Liu, M. B. Johnston and H. J. Snaith, *Nature*, 2013, **501**, 395–398.

4 L. Yu, S. Lany, R. Kykyneshi, V. Jieratum, R. Ravichandran, B. Pelatt, E. Altschul, H. A. S. Platt, J. F. Wager, D. A. Keszler and A. Zunger, *Adv. Energy Mater.*, 2011, **1**, 748–753.

5 K. Woo, Y. Kim and J. Moon, *Energy Environ. Sci.*, 2012, **5**, 5340–5345.

6 S. Chen, A. Walsh, A. X.-G. Gong and S.-H. Wei, *Adv. Mater.*, 2013, **25**, 1522–1539.

7 K. Zeng, D.-J. Xue and J. Tang, *Semicond. Sci. Technol.*, 2016, **31**, 063001.

8 Y. Zhou, M. Leng, Z. Xia, J. Zhong, H. Song, X. Liu, B. Yang, J. Zhang, J. Chen, K. Zhou, J. Han, Y. Cheng and J. Tang, *Adv. Energy Mater.*, 2014, **4**, 1301846.

9 Y.-Q. Liu, M. Zhang, F.-X. Wang and G.-B. Pan, *J. Mater. Chem. C*, 2014, **2**, 240–244.

10 H.-J. Wu, P.-C. Lee, F.-Y. Chiu, S.-W. Chen and Y.-Y. Chen, *J. Mater. Chem. C*, 2015, **3**, 10488–10493.

11 J. Yang, Y. Lai, Y. Fan, Y. Jiang, D. Tang, L. Jiang, F. Liu and J. Li, *RSC Adv.*, 2015, **5**, 85592–85597.

12 Y. Kuang, M. D. Vece, J. K. Rath, L. V. Dijk and R. E. I. Schropp, *Rep. Prog. Phys.*, 2013, **76**, 106502.

13 A. I. Hochbaum and P. Yang, *Chem. Rev.*, 2010, **110**, 527–546.

14 P. V. Kamat, K. Tvrdy, D. R. Baker and J. G. Radich, *Chem. Rev.*, 2010, **110**, 6664–6688.

15 G.-Y. Chen, B. Dneg, G.-B. Cai, T.-K. Zhang, W.-F. Dong, W.-X. Zhang and A.-W. Xu, *J. Phys. Chem. C*, 2008, **112**, 672–679.

16 J. Ma, Y. Wang, Y. Wang, Q. Chen, J. Lian and W. Zheng, *J. Phys. Chem. C*, 2009, **113**, 13588–13592.

17 T. Zhai, M. Ye, L. Li, X. Fang, M. Liao, Y. Li, Y. Koide, Y. Bando and D. Golberg, *Adv. Mater.*, 2010, **22**, 4530–4533.

18 Y. H. Kwon, M. Jeong, H. W. Do, J. Y. Lee and H. K. Cho, *Nanoscale*, 2015, **7**, 12913–12920.

19 Y. Liang, Y. Wang, J. Wang, S. Wu, D. Jiang and J. Lian, *RSC Adv.*, 2016, **6**, 11501–11506.

20 C.-H. Chung, S.-H. Li, B. Lei, W. Yang, W. W. Hou, B. Bob and Y. Yang, *Chem. Mater.*, 2011, **23**, 964–969.

21 Y. Oh, W. Yang, J. Kim, K. Woo and J. Moon, *ACS Appl. Mater. Interfaces*, 2015, **7**, 22570–22577.

22 Y. Zhou, L. Wang, S. Chen, S. Qin, X. Liu, J. Chen, D.-J. Xue, M. Luo, Y. Cao, Y. Cheng, E. H. Sargent and J. Tang, *Nat. Photonics*, 2015, **9**, 409–415.

23 M.-Z. Xue and Z.-W. Fu, *J. Alloys Compd.*, 2008, **458**, 351–356.

24 Y. Rodriguez-Lazcano, Y. Peña, M. T. S. Nair and P. K. Nair, *Thin Solid Films*, 2005, **493**, 77–82.

25 Z. Deng, D. Chen, F. Tang and M. Mansuripur, *Cryst. Growth Des.*, 2009, **4**, 1823–1828.

26 S. Biswas, S. Kar and S. Chaudhuri, *Appl. Surf. Sci.*, 2007, **253**, 9259–9266.

27 P. G. Sheikhiabadi, M. Salavati-Niasari and F. Davar, *Mater. Lett.*, 2012, **71**, 168–171.

28 Y. Yang, G. Wang, W. Zhao, Q. Tian, L. Huang and D. Pan, *ACS Appl. Mater. Interfaces*, 2015, **7**, 460–464.

29 M. Janecek and R. Kral, *Modern Electron Microscopy in Physical and Life Sciences*, InTech, Rijeka, 2016.

30 N. Guijarro, M. S. Prévot and K. Sivula, *Phys. Chem. Chem. Phys.*, 2015, **17**, 15655–15674.

31 X. Liu, J. Chen, M. Luo, M. Leng, Z. Xia, Y. Zhou, S. Qin, D.-J. Xue, L. Lv, H. Huang, D. Niu and J. Tang, *ACS Appl. Mater. Interfaces*, 2014, **6**, 10687–10695.

32 N. Guijarro, M. S. Prevot, X. Yu, X. A. Jeanbourquin, P. Bornoz, W. Bouree, J. Johnson, F. L. Formal and K. Sivula, *Adv. Energy Mater.*, 2016, 1501949.

33 C. Fàbrega, T. Andreu, A. Tarancón, C. Flox, A. Morata, L. Calvo-Barrio and J. R. Morante, *Int. J. Hydrogen Energy*, 2013, **38**, 2979–2985.

34 Y.-C. Wang, C.-Y. Chang, T.-F. Yeh, Y.-L. Lee and H. Teng, *J. Mater. Chem. A*, 2014, **2**, 20570–20577.

35 Z. Liu and L. Yan, *Phys. Chem. Chem. Phys.*, 2016, **18**, 31230–31237.

36 C. Li, T. Hisatomi, O. Watanabe, M. Nakabayashi, N. Shibata, K. Domen and J.-J. Delaunay, *Appl. Phys. Lett.*, 2016, **109**, 033902.

37 L. Rovelli, S. D. Tilley and K. Sivula, *ACS Appl. Mater. Interfaces*, 2013, **5**, 8018–8024.

38 L. Zhang, T. Minegishi, J. Kubota and K. Domen, *Phys. Chem. Chem. Phys.*, 2014, **16**, 6167–6174.

39 M. Moriya, T. Minegishi, H. Kumagai, M. Katayama, J. Kubota and K. Domen, *J. Am. Chem. Soc.*, 2013, **135**, 3733–3735.

40 C. G. Morales-Guio, S. D. Tilley, H. Vrubel, M. Gratzel and X. Hu, *Nat. Commun.*, 2014, **5**, 3059.

41 F. Jiang, Gunawan, T. Harada, Y. Kuang, T. Minegishi, K. Domen and S. Ikeda, *J. Am. Chem. Soc.*, 2015, **137**, 13691–13697.